Delft University of Technology

Document Version
Final published version

Licence
Dutch Copyright Act (Article 25fa)

Citation (APA)
Khazem, R., Colin, J., Shi, H., Casalinho, J., Schott, D., & Puel, F. (2026). Characterization of wood powder properties: A DEM-based calibration with rotating drum experiments. *Powder Technology*, *473*, Article 122157. https://doi.org/10.1016/j.powtec.2026.122157

Important note
To cite this publication, please use the final published version (if applicable). Please check the document version above.

Copyright
In case the licence states "Dutch Copyright Act (Article 25fa)", this publication was made available Green Open Access via the TU Delft Institutional Repository pursuant to Dutch Copyright Act (Article 25fa, the Taverne amendment). This provision does not affect copyright ownership.
Unless copyright is transferred by contract or statute, it remains with the copyright holder.

Sharing and reuse
Other than for strictly personal use, it is not permitted to download, forward or distribute the text or part of it, without the consent of the author(s) and/or copyright holder(s), unless the work is under an open content license such as Creative Commons.

Takedown policy
Please contact us and provide details if you believe this document breaches copyrights.
We will remove access to the work immediately and investigate your claim.

This work is downloaded from Delft University of Technology.

Powder Technology 473 (2026) 122157

Contents lists available at ScienceDirect

Powder Technology

journal homepage: www.journals.elsevier.com/powder-technology

Characterization of wood powder properties: A DEM-based calibration with rotating drum experiments

Reem Khazem [a], Julien Colin [a,b], Hao Shi [c], Joel Casalinho [a], Dingena Schott [c], François Puel [a,*]

[a] *Université Paris-Saclay, CentraleSupélec, Laboratoire de Génie des Procédés et Matériaux, 91190 Gif-sur-Yvette, France*
[b] *Laboratoire Réactions et Génie des Procédés, CNRS, Université de Lorraine, 54000, France*
[c] *Department of Maritime and Transport Technology, Faculty of Mechanical Engineering, Delft University of Technology, 2628CD Delft, the Netherlands*

HIGHLIGHTS

- DEM simulation of wood powders (spruce and poplar) in a rotating drum.
- Novel calibration method via a digital twin with new flow descriptors.
- Rolling, sliding friction and cohesion energy density (μ_r, μ_s, CED) are calibrated.
- Higher cohesion in spruce linked to fibrous rough surface, using image analysis.
- Influence of (μ_r, μ_s, CED) on unconfined powder flowability was investigated.

GRAPHICAL ABSTRACT

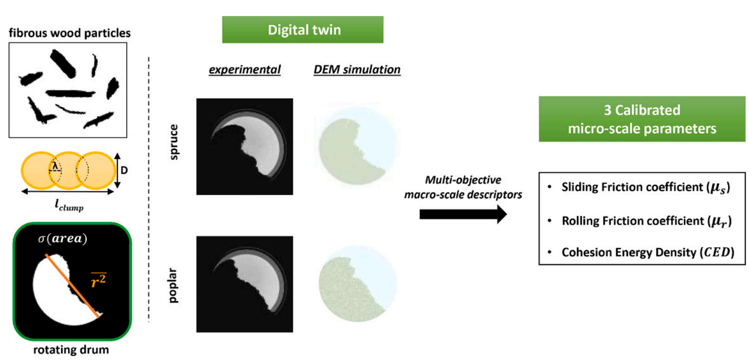

ARTICLE INFO

Keywords:
Powder
Woody biomass
Discrete Element Method
Cohesion
Friction
Flowability
Particle shape

ABSTRACT

Powder flowability underlies reliable solids handling, influencing dosing accuracy and production stability. Wood powders are usually cohesive and susceptible to flow problems like bridging because of their irregular, fibrous particles that are hygroscopic and heterogeneous. Two lignocellulosic powders were tested: spruce (softwood) and poplar (hardwood). Their particle size distribution, particle shape, and density were measured experimentally. Crucially, the interparticle parameters that govern powder bulk behavior, which are the cohesion energy density (*CED*), rolling friction coefficient (μ_r), and sliding friction coefficient (μ_s), are not directly measurable at the scale and morphological complexity of fibrous wood particles. Therefore, using the Discrete Element Method (DEM), (μ_s, μ_r, *CED*) were identified as effective DEM parameters by inverse calibration against rotating drum tests. A novel calibration workflow was developed to compare DEM simulations with real rotating drum experiment indicators, which can be used for unconfined, dynamic flow. These indicators correspond to newly discovered macroscopic flow descriptors that are processed from the powder bed: average projected area $\overline{Area}$, its fluctuation $\sigma(Area)$, and the average surface profile irregularity $\overline{r^2}$. Wood particles were modeled as multi-sphere clumps with different sizes to balance realism and computational cost. The calibrated parameters were: spruce—μ_s=0.10, μ_r=0.367, CED=130 kJ/m^3; poplar—μ_s=0.10, μ_r=0.772, CED=100 kJ/m^3. Following a comprehensive results analysis, increasing CED and friction parameters deteriorates powder unconfined

* Corresponding author.
E-mail address: francois.puel@centralesupelec.fr (F. Puel).

https://doi.org/10.1016/j.powtec.2026.122157
Received 5 November 2025; Received in revised form 14 January 2026; Accepted 16 January 2026
Available online 21 January 2026
0032-5910/© 2026 Elsevier B.V. All rights reserved, including those for text and data mining, AI training, and similar technologies.

flowability by promoting agglomeration and particle interlocking. The resulting calibrated DEM inputs provide a baseline for predicting and improving the handling of wood powders in hoppers, feeders, and conveying screws.

1. Introduction

Wood is increasingly processed in biorefineries to produce bio-based fuels and chemicals; therefore, reliable handling of biomass powders is fundamental to scaling the bioeconomy [1]. In biorefineries, wood powders are stored and fed into units like torrefaction, pelletizing, pyrolysis, gasification, and enzymatic hydrolysis. Yet, unlike near-ideal granular media such as glass beads, wood powders are irregular, lightweight, and cohesive. Their particles often exhibit fibrous surfaces and broad size distributions, which together produce behaviors like arching, ratholing, and intermittent discharge that are hard to predict and costly to control in feeders, hoppers, conveying screws and reactors. These flowability issues translate directly into energy losses, downtime, and off-spec product [2].

Flowability assessment of granular material has lately gained increasing interest. There are several techniques to evaluate powder flowability, relative movement of a bulk of particles, which can be classified into confined or unconfined flow. While shear cells and uniaxial testers characterize powder behavior under confined conditions (under stress) [3], rotating drums are better suited for studying unconfined powder flow, where free-surface dynamics dominate [4]. Rotating drums are cylinders partially filled with powder, rotated at a certain speed, and coupled with image acquisition to capture frames of the powder bed. In our previous research, we determined new efficient and reliable flow descriptors through image processing [5]. The flow descriptors used in this work are the powder bed surface linearity r^2 and fluctuation of the projected area $\sigma(Area)$. We studied the flowability of two types of wood powder: spruce (softwood) and poplar (hardwood).

Understanding the powder properties governing their flow behavior is very important [6–9]. Morphological properties for these two powders were measured through experimental tools, like size, shape and surface texture, and density. Morphology clearly matters, but it's not the sole player for explaining the different flowability between the spruce and poplar samples. Surface and cohesion properties like sliding friction coefficient (μ_s), rolling friction coefficient (μ_r), and cohesion energy density between particles (CED) have a significant impact on the powder flow. In order to estimate these properties, Discrete Element Method (DEM) was used. DEM is a numerical simulation tool that models the bulk solid as individual particles and computes their forces, positions, collisions and different interactions step by step [10]. It is interesting because it links particle-scale parameters to observable bulk behavior, enables safe hypothetical tests that are hard or costly in the lab, and yields more predictive models for real processes. We note that while single-contact methods such as the atomic force microscopy (AFM) colloidal-probe or lateral-force microscopy can probe particle–particle sliding friction μ_s, the measured values are highly sensitive to surface roughness, humidity, and loading history and therefore are not directly transferable to bulk flow [11]. Rolling friction μ_r at the particle scale is even more elusive for sub-millimetric, irregular lignocellulosic particles; it acts as an effective resistance emerging from shape-induced interlocking, micro-slip, and asperity deformation, and there is no broadly accepted, ensemble-representative direct test. [12]. Likewise, cohesion energy density (CED) in DEM contact laws is a lumped, model-dependent parameter that maps attractive forces (van der Waals, capillary, electrostatics) across rough, non-spherical contacts to a bulk-effective cohesion; although proxies such as surface energy (inverse gas chromatography) and pull-off forces (AFM) can be measured, converting them to a unique CED requires assumptions about contact mechanics and roughness statistics [13]. J. Pachón et al. used DEM to calibrate (μ_s, μ_r, CED) of wood powder based on simulating bulk tests and measuring three physical responses – static angle-of-repose from heap formation, bulk density, and retainment ratio by the rectangular container test (ledge test) [14]. However, no biomass particles were observed to flow when the lid of the rectangular container was lifted, stable stacks of particles were formed because of interlocking and interparticle cohesive forces, so the authors assigned the retainment ratio to be 1. Consequently, this test appears less representative for fibrous or cohesive powders such as biomass. A recent research studied the sensitivity of μ_s, μ_r, CED, and CoR (coefficient of restitution) on different DEM digital twins of powder characterization tools, including GranFlow, GranuHeap, and GranuDrum, but without performing any calibration [15].

Several particle shape representations exist in DEM, ranging from ideal spheres to clumped or polyhedral forms and other complex shapes, but these approaches often come with a trade-off between accuracy and computational cost [16]. Despite their industrial relevance, wood powders are under-represented in DEM studies compared with pelletized biomass. In recent literature, Zakia Tasnim et al. employed a clumped-sphere representation to model pine residues, but with particle sizes around 4 mm, whereas Józef Horabik et al. represented wood sawdust using single spherical particles [17,18]. Both studies targeted simulations other than rotating-drum experiments. In the current work, wood particles were approximated using a multisphere representation, combined with a size-scaling strategy to keep simulation times manageable while preserving realistic morphology. Experimentally measured particle size distributions were used as inputs to the model. To calibrate the model and reach the correct combination (CED, μ_s, μ_r) for spruce and poplar samples, systematic simulations were performed and calibrated with the real rotating drum experiment outputs of each sample with the help of a Design of Experiments. Based on the powder bed surface linearity and its projected area, an objective function was formulated to optimize the (CED, μ_s, μ_r) triplet by minimizing the sum of the normalized discrepancies between simulated and experimental results. By systematically varying these surface and cohesion parameters in DEM simulations, their individual and combined roles in influencing unconfined powder flowability were revealed, providing insights into which mechanisms dominate for such materials.

This study introduces a novel calibration framework that integrates rotating drum experiment with DEM simulations to extract key surface interaction parameters—cohesion energy density (CED), sliding friction (μ_s), and rolling friction (μ_r)—based on new descriptors of the powder bed dynamics. These effective DEM parameters provide insights for simulating and optimizing the flow behavior in feeding, conveying, and reactor charging operations.

2. Materials and methods

2.1. Wood powder: preparation and characterization

Two wood powders were studied: spruce (*Picea abies (L.)*) as the softwood and poplar (*Populus euro-americana 'Koster'*) as the hardwood. Spruce was selected for its widespread use in forestry and relevance to biomass-to-liquid (*BtL*) processes; samples came from a plantation in the *Le* Châtaignier forest (Riotord, France). Poplar was chosen for its fast growth in temperate climates and suitability as an energy crop; samples were taken from the La Suippe valley near Auménancourt-le-Petit (France) [19,20]. The average growth-ring width was 2.85 mm for spruce and about 14 mm for poplar.

Dry boards from each species were cut into $60 \times 80 \times 15$ mm^3 chips and milled to powder using a cutting mill (*Retsch SM 300*) at 1500 rpm. To limit heat build up from grinding, each batch was processed in two passes. Material first passed a 10 mm trapezoidal-hole bottom sieve and then a 1 mm sieve. The resulting powder was fractionated on a vibratory sieve shaker (*Retsch® AS 200*) for 20 min at 60 Hz, and the [500–800] μm sieve cut was used in this work. These powders were stored in plastic bags and kept under ambient laboratory conditions (room atmosphere).

The wood particle morphology was characterized with a dynamic image analyzer (*Sympatec QICPIC*), using the M7 lens (measurement range 10–10,240 μm) together with the GRADIS dispersion and VIBRI feeding units [21]. The instrument software processed the images to extract particle size and shape metrics. Because wood particles are highly irregular, we used Feret diameters as size descriptors—the distances between two parallel tangents on opposite sides of a particle's contour (Fig. 1). We report the maximum (F_{max}), minimum (F_{min}), and mean (F_{mean}) Feret diameters. For shape, we focus on measuring particle circularity. Circularity ($0 < \psi \leq 1$) is defined as the ratio of the equivalent perimeter, P_{eq} (that of a disk with the same projected area A_p), to the measured perimeter P_{real} (Eq. (1)):

$$\psi = \frac{P_{eq}}{P_{real}} = \frac{2\sqrt{\pi \cdot A_p}}{P_{real}} \tag{1}$$

A value of ψ=1 corresponds to a perfect circle in projection. As ψ decreases, the shape becomes more elongated and/or irregular. Rough, jagged edges increase P_{real} without changing A_p, which lowers ψ; therefore, for the same area, a smoother particle has a higher circularity than a rougher one.

2.2. Rotating drum: unconfined flowability

Wood-powder flowability was evaluated with a customized rotating drum, following the protocol in our earlier study [5]. The device consists of a stainless-steel cylinder (inner diameter 10 cm, width 2 cm) with an internal roughness of ~0.4 μm, enclosed by two transparent glass windows whose inner faces carry a very thin conductive coating (Fig. 2a). For each test, the drum was filled with a 20π cm^3 cylindrical container of powder, which is 40% of the drum volume, and rotated at 1 rpm. Powder motion was captured using a high-speed camera (*Photron® FASTCAM, Mini AX100*) paired with a 105 mm f/2.8 macro lens (*SIGMA®, EX DG Macro OS*). A backlight panel (*PHLOX®, LEDWBL*, 200 × 200 mm^2, 24 V) behind the drum provided uniform, high-contrast illumination. Images were recorded at 50 fps with a resolution of 1024 × 1024 pixels and an exposure time of 1/60,000 s (Fig. 2b).

A MATLAB code was written to process these images and calculate several flow descriptors [5]. For each sample in the drum, the projected area (*Area*) and the irregularity of the surface profile (r^2) were calculated through rotating time (Fig. 2c). The *Area* is calculated by binarizing the grey images of the rotating drum, deleting any pixel outside the drum cylinder circumference, and counting the number of pixels corresponding to the granular bed using the "*bwarea*" function in Matlab. During rotation, the *Area* fluctuates, so its average value is calculated and also its standard deviation σ(Area) along rotating time. r^2 is calculated by fitting a line through the profile (interface between the powder bed and air) using *Principal Component Regression* (PCR), and not linear

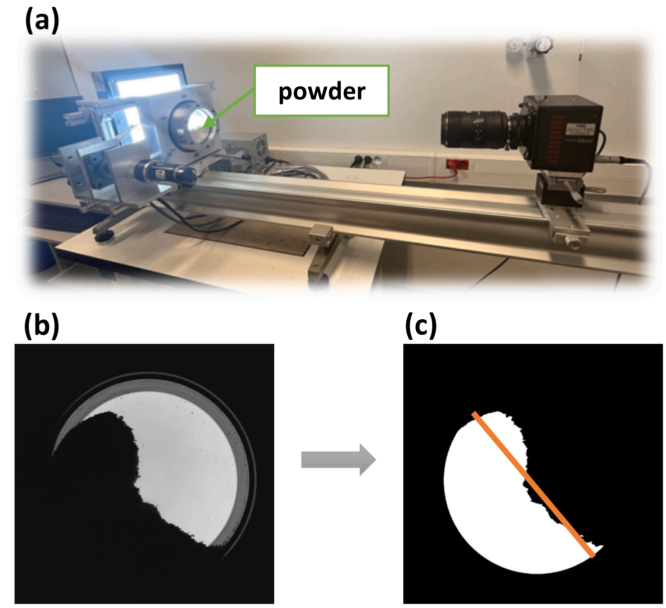

Fig. 2. (a) Rotating drum setup. (b) Typical image of spruce powder captured by the camera. (c) Illustration of the projected powder area (white) and the surface fitting line (orange).

regression, following the equation below:

$$r^2 = 1 - \frac{\sum_{i=1}^{N} (d_i)^2}{\sum_{i=1}^{N} \left[(y_i - \bar{y})^2 + (x_i - \bar{x})^2 \right]} \tag{2}$$

$$\begin{cases} \hat{y}'_i = a\, x_i + b \Longleftrightarrow \hat{x}'_i = \dfrac{y_i}{a} - \dfrac{b}{a} \\ d_i = \dfrac{|a\, x_i - y_i + b|}{\sqrt{a^2+1}} = \dfrac{|\hat{y}'_i - y_i|}{\sqrt{a^2+1}} = \dfrac{|\hat{x}'_i - x_i|}{\sqrt{\left(1/a\right)^2 + 1}} \end{cases} \tag{3}$$

where:

- (x_i, y_i) are the experiment profile points of the powder bed,
- $(x_i, \hat{y}_i)$ belong to the fitting regression line having slope (a) and ordinate axis-intercept (b),
- d_i is the Euclidean distance, minimum distance between the regression line and experimental points. As a result, PCR is mathematically independent of variations induced by drum rotation, unlike when using a linear distance, making it a robust descriptor for quantifying surface irregularity in rotating-drum experiments.

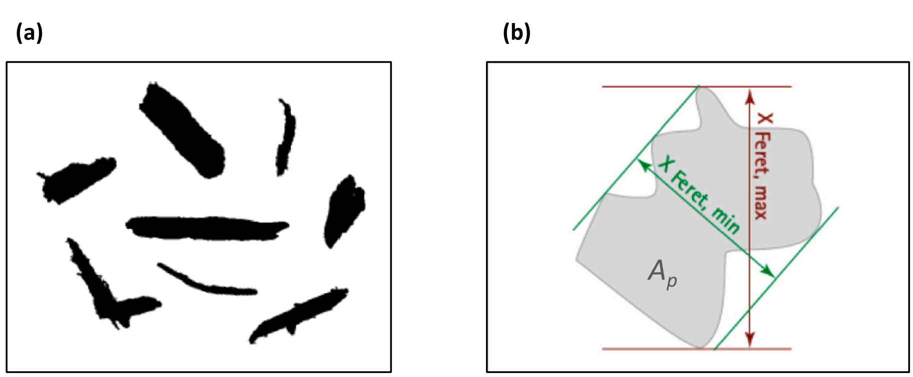

Fig. 1. (a) Example pictures of wood particles taken by QICPIC. (b) Representation of Feret diameters [22].

Finally, powder with better flowability has higher interface linearity $\overline{r^2}$ and lower fluctuation in the bulk area $\sigma(Area)$ [5].

2.3. Discrete Element Method

To simulate the motion of wood powder in the rotating drum, we performed Discrete Element Method (DEM) simulations in Altair® EDEM 2024.1 using the GPU-accelerated CUDA solver [23].

2.3.1. Contact model

Hertz–Mindlin (no-slip) contact law was used to model particle contacts, which captures elastic normal and tangential interactions and accounts for energy dissipation via damping [24,25]. Fig. 3 shows an illustration of the forces acting between two spheres in contact [26]. To represent the limited free rotation of the irregular wood particles, this was coupled with the *Type-C rolling-friction* model, which applies a resisting torque to mimic non-spherical particle shape [27].

Because wood powders are cohesive, we also included an attractive-force model namely *Linear Cohesion V2,* to reproduce interparticle adhesion. These forces are a function of the material cohesion energy density and the particle overlap [28].

Table 1 summarizes the main equations used by the DEM model, which accounts for the *Hertz–Mindlin (no-slip)* contact law with *Type-C rolling-friction* model and *Linear Cohesion V2.*

2.3.2. Particles and drum modeling

Wood powder particles are highly irregular because of their fibrous origin, often resembling elongated needles or splinters rather than compact grains. To capture this anisotropy without the overhead of complex surface meshing, each particle was modeled as a multisphere (clumped-sphere) assembly: a small set of overlapping spheres aligned along a common longitudinal axis. This construction preserves the essential geometry while keeping contact detection robust. Although polygonal or voxelized particles can reproduce fine edges more accurately, they come with much higher computational cost [29]. The multisphere approach showed a practical balance between realism and efficiency, which made it suitable for simulating hundreds of thousands of cohesive particles moving in the rotating drum. It's important to note that including cohesion in the DEM model increases computational cost, as additional adhesive force calculations and longer-lasting particle contacts require more simulation time compared to non-cohesive particles [30].

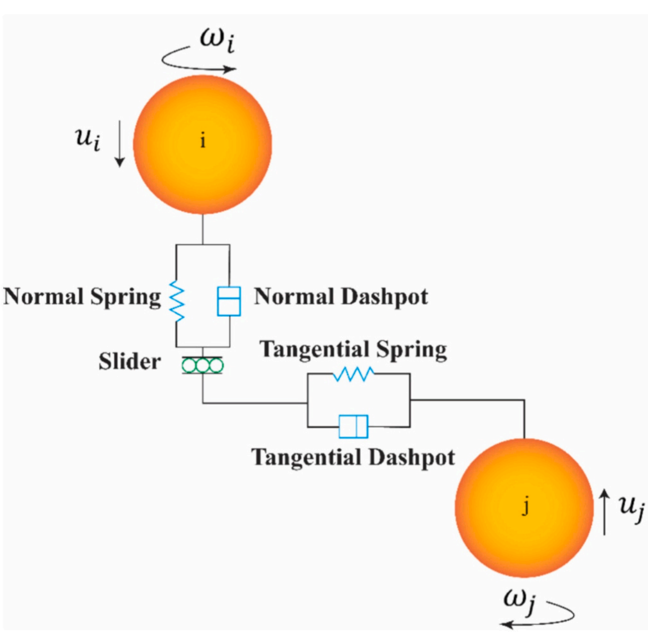

Fig. 3. Schematic representationof the forces interacting between two particles in DEM [26].

Table 1
Equations used by the DEM models.

Normal force with damping	$F_n = \frac{4}{3}E^*\sqrt{R^*}\delta_n^{3/2} - 2\sqrt{\frac{5}{6}}\beta\sqrt{S_n m^*}\overrightarrow{v_n^{rel}}$
Tangential force with damping	$F_t = -S_t\delta_t - 2\sqrt{\frac{5}{6}}\beta\sqrt{S_t m^*}\overrightarrow{v_t^{rel}}$; $\lvert F_t\rvert \leq \mu_s \cdot \lvert F_n\rvert$
Damping torque (viscous and non-viscous)	$M_r = -K_r\theta_r - 2\eta\sqrt{I_r k_r}\omega$; $\lvert -K_r\theta_r\rvert \leq \mu_r R_r F_n$
Cohesive force	$F_{coh} = CED \cdot A$

Where δ_n - normal overlap, E^*- effective Young's modulus, R^*- effective radius, m^* - the equivalent mass, v_n^{rel} - the normal component of the relative velocity, S_n - the normal stiffness, $\beta = \frac{-\ln e}{\sqrt{\ln^2 e + \pi^2}}$, e - the coefficient of restitution, δ_t - the tangential overlap, S_t - the tangential stiffness, μ_s - the coefficient of static friction, K_r - the rolling stiffness, θ_r - the relative rotation angle, R_r - the equivalent rolling radius, μ_r - the Coefficient of Rolling Friction, η - the rolling viscous damping ratio, I_r - the equivalent Moment of Inertia for the rotational vibration mode about the contact point, ω - the relative rotational velocity vector at the contact point, CED - the Cohesion Energy Density, and A - the particles' contact area.

Fig. 4 illustrates the representation of particles using clumped spheres, where D is the diameter, l_{clump} is the length of the clump (particle) and λ is the overlap between the spheres. The overlapping factor 'c' can be expressed as $c = \frac{\lambda}{D}$, meaning that the spheres are in contact at a single point when $c = 0$ while they totally overlap each other when $c = 1$. As c increases, the effective surface roughness of the particle decreases. In this work, a value of $c = 0.2$ (20%) was selected, as it provides a suitable compromise between representation accuracy and computational efficiency in terms of the number of spheres required [14,31].

First, we constructed a clump that approximates the average particle shape and size derived from the experimental image-analysis data for each sample. The average minimum and maximum Feret diameters calculated by the particle analyzer are used, which are noted by $\overline{F_{min}}$ and $\overline{F_{max}}$ respectively. The following rule was followed to calculate the number of spheres (n) of the reference clump:

$$\begin{cases} \mathrm{D} = \overline{\mathrm{F_{min}}} \\ (\mathrm{l_{clump}})_0 = \overline{\mathrm{F_{max}}} = \mathrm{n}.(\mathrm{D} - \lambda) + \lambda \end{cases}$$

consequently $n = \frac{\frac{\overline{F_{max}}}{\overline{F_{min}}} - c}{1 - c}$.

Since the number of spheres can't be a decimal, the integer value of n is considered and the length of the clump is recalculated again using the rounded n value: $l_{clump} = n.(\mathrm{D} - \lambda) + \lambda$.

Concerning the 1st sample, spruce, $\overline{F_{min}} = 653.95$ µm and $\overline{F_{max}} = 1773.11$ µm, so n=3.1, which is considered as 3 spheres (Fig. 5). Thus,

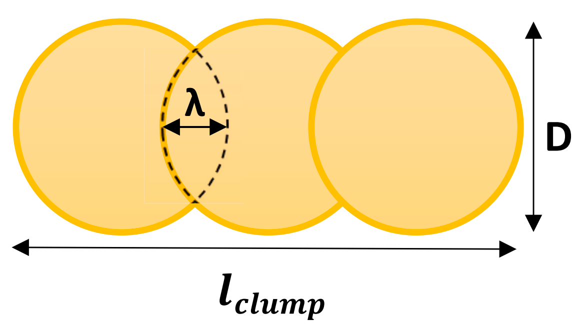

Fig. 4. Multi-sphere particle representation.

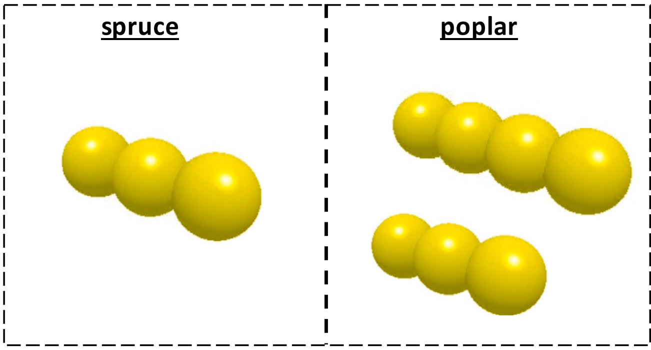

Fig. 5. Particle shape representation of the two wood powder samples on EDEM.

the length of the clump is 1700.3 µm. As for the 2nd sample, poplar, $\overline{F_{min}}$ = 624.78 µm and $\overline{F_{max}}$ = 1841.41 µm, so n=3.43. In order to give good representation of this wood powder, the target average n=3.43 was achieved by mixing 3-sphere and 4-sphere clumps. The fractions were computed from the weighted-average relation $n = 3f_3 + 4f_4$ with $f_3 + f_4 = 1$,where f_3 and f_4 represent the fraction of particles modeled as 3-sphere clumps and 4-sphere clumps respectively. Thus, $f_3 = 0.57$ and $f_4 = 0.43$.Accordingly, 57% of particles were represented by 3-sphere clumps (l_{clump}= 1624.4 µm) and 43% by 4-sphere clumps (l_{clump}= 2124.2 µm).

Both wood powders were initially sieved using a mesh with openings of 500–800 µm, which refers to the hole size of the sieve rather than the actual particle size. In a next step, particle-size polydispersity was introduced based on measurements obtained with a QICPIC dynamic image analysis system. The resulting particle size distribution (PSD) is shown in Fig. 6, where particle size is reported as the mean Feret diameter (F_{mean}). Simulating the full continuous PSD would be computationally prohibitive; therefore, the PSD was discretized into three representative size classes. Each class was assigned a mass fraction corresponding to the measured PSD, and a representative size for that class was defined from the particle analyzer data.

To implement these classes in DEM, the representative size of each class was expressed relative to the reference particle previously used to match the average particle shape (i.e., the monodisperse 'reference' particle described above). The particle volume was then scaled accordingly (i.e., all sphere radii within the clump were multiplied by a constant factor for that class), while the clump topology (number and arrangement of spheres) was kept unchanged.

For spruce, the three increasing size classes (small → medium → large) accounted for 16%, 68%, and 16% of the total mass and were implemented using volume scaling factors of 0.6, 1.0 (no scaling), and 1.8, respectively, applied to the spruce reference clump (3-sphere clump). For poplar, the same mass fractions (16%, 68%, and 16%) were used, with volume scaling factors of 0.7, 1.0, and 1.5, respectively. These scaling factors were applied to the previously defined poplar clump library (mixture of 3-sphere and 4-sphere clumps), thereby preserving the calibrated shape representation while introducing size polydispersity. The summary of the final particles representations for spruce and poplar are present in Table 2.

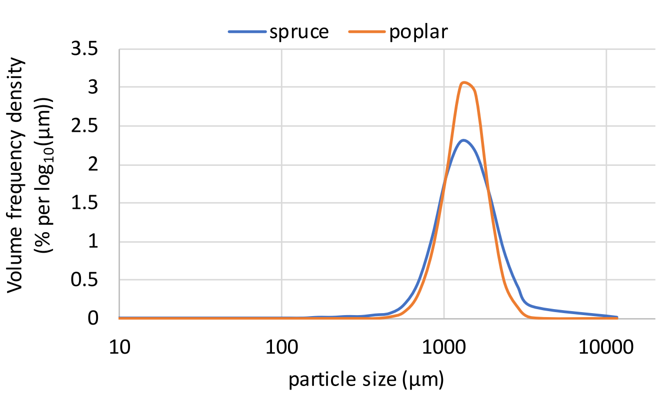

Fig. 6. Differential volume-based distribution of particle size (F_{mean}) for spruce and poplar samples generated by the QICPIC.

The density of the materials was set to 428 kg/m^3 for spruce and 373 kg/m^3 for poplar (Table 3). Since the particles of each powder sample are non-uniform, those values were chosen based on measuring the densities of the wood chips, at equilibrium moisture content (EMC), before grinding. The mass of each chip was recorded, and its volume was determined using Archimedes' principle [32]. The wood chip was completely immersed in a container of water without touching the bottom or sides. The mass of displaced water was recorded on a balance and converted to volume using the water density. Although this method is usually applied to fully water-saturated wood to calculate infra-density, our aim was to determine density at equilibrium moisture content (EMC). Since water could seep into the pores during immersion and affect the result, the chips were first sprayed with a thin waterproof coating. The coating volume was negligible. As for the bulk density values, they were obtained experimentally by weighing a separate container filled with powder prior to loading the rotating drum and used to calculate the total mass of the generated particles in the simulations.

Concerning the rotating drum, it was modeled as a rigid cylinder using its real dimensions (diameter 10 cm, width 2 cm). Boundary materials were assigned to match the setup: the drum walls were defined as stainless steel and the other contacting disk surfaces as glass. The drum was driven at a constant rotational speed of 1 rpm for all simulations.

Table 3 summarizes some properties that were used for the DEM simulations. The values accompanied by (*) are measured experimentally at the lab, while others are based on literature [33,34].

The simulation time step Δt, time between iterations of the Euler integration, was set to 25% of the Rayleigh time step. The Rayleigh time step is the characteristic time associated with a surface (Rayleigh) elastic wave propagating across the smallest particles; it depends on the particle size and material properties (e.g., density, Young's modulus, and Poisson's ratio) [35]. Using a quarter of this limit is a common, conservative choice because it reduces numerical oscillations and nonphysical overlaps while keeping the simulation efficient. The time step for spruce simulations was 4.39877e-06 s and that for poplar was 4.13011e-06 s.

Table 2
Final DEM particle representations used in simulations.

Wood	Size class	PSD mass fraction (%)	Final particle-shape representation	Final $l_{clump,final}$ (µm)
Spruce	Small	16	100% clumps with $n = 3$ spheres	1434.1
	Medium	68	100% clumps with n = 3 spheres	1700.3
	Large	16	100% clumps with n = 3 spheres	2068.3
Poplar	Small	16	57% clumps with n = 3 + 43% clumps with $n = 4$	n = 3: 1442.3 n = 4: 1886.1
	Medium	68	57% clumps with n = 3 + 43% clumps with n = 4	n = 3: 1624.4 n = 4: 2124.2
	Large	16	57% clumps with n = 3 + 43% clumps with n = 4	n = 3: 1859.5 n = 4: 2431.6

Table 3
Parameters used for EDEM simulations.

	Spruce *(s)*	Poplar *(p)*	Drum lateral wall *(w)*	Drum disks *(d)*
Poisson ratio	0.3	0.3	0.3	0.22
Young's Modulus, Pa	5.00E+06	5.00E+06	1.93E+11	1.00E+09
Coefficient of Restitution with granular material: *spruce*	*s-s*: 0.1	–	*w-s*: 0.1	*d-s*: 0.5
Coefficient of Restitution with granular material: *poplar*	–	*p-p*: 0.1	*w-s*: 0.1	*d-s*: 0.5
Particle/ material density, kg/m^3	428*	373*	8000	2500
Bulk density, kg/m^3	131*	205*	–	–

2.3.3. Scaling impact study

To save computational time, a scaling study was carried out first before conducting a full design-of-experiments (DoE) of simulations. The dimensions of the rotating drum were kept the same, but the volume of the particles was scaled by 2, keeping the same filling ratio of the powder in the drum. This approach is called coarse-graining, which decreases the time of simulation as the number of generated particles will decrease [36]. However, the impact of this scaling approach on the results has to be assessed, thus random combinations of CED, μ_s, and μ_r were tested for the spruce sample. Table 4 shows the different tests simulated; each test was performed twice, one without scaling (*scale 1*) and one with scaling (*scale 2*). For each case, the powder average area with its standard deviation ($\overline{Area}$, $\sigma(Area)$) and the average irregularity of the surface profile ($\overline{r^2}$) were calculated and compared (Fig. 7).

Across tests A to D, the adopted scaling generally preserved similar results and trends of the rotating drum outputs. The differences observed between the scaled and unscaled simulations are not very significant but vary depending on the input parameters, indicating that there is no single uniform formula to accurately transform the results from scale 2 back to scale 1. This scaling is effective because it showed a notable reduction in computation time, from approximately 13 h to around 6 h, while preserving the relevant physics. The particles' volume was increased while conserving the geometry and shape of particle assemblies, and the drum geometry, fill fraction, and Froude number F_r that influences the flow regime were held constant ($F_r = \frac{(angular\ velocity)^2 \cdot (drum\ radius)}{g}$) [37]. In this study we focused on a comparative, scaled-level calibration of spruce and poplar to compare and study the effects of (CED, μ_s, μ_r), so the assembly of particles representing each of the spruce and poplar samples was volume-scaled by a factor of 2. Future work will focus on quantifying scaling effects explicitly and testing the transferability of *CED*, μ_s, and μ_r across scales. It is worth noting that different scaling strategies were initially tested such as scaling up the particle size by higher values or scaling down the rotating drum size, but the approach presented here yielded the best results.

2.3.4. Calibration approach

To identify the optimal (CED, μ_s, μ_r) combination of each wood powder, a calibration procedure was developed and is summarized in Fig. 8. The main goal is to have similar results between the real rotating drum experiments and the simulated tests on DEM. The condition for the KPIs, key performance indicators, in this study was to reach: $|\overline{Area_{sim}} - \overline{Area_{exp}}| \leq 1$, $|\sigma(Area)_{sim} - \sigma(Area)_{exp}| \leq 0.1$, $|\overline{r^2}_{sim} - \overline{r^2}_{exp}| \leq 0.01$; where '*sim*' corresponds to the simulated results and '*exp*' to the experimental ones. Based on this condition, the best simulation is the one exhibiting the minimum value of the objective function '$f(\text{CED}, \mu_s, \mu_r)$' which is as follows:

$$f(\text{CED}, \mu_s, \mu_r) = \frac{|\overline{Area_{sim}} - \overline{Area_{exp}}|}{\overline{Area_{exp}}} + \frac{|\sigma(Area)_{sim} - \sigma(Area)_{exp}|}{\sigma(Area)_{exp}} + \frac{|\overline{r^2_{sim}} - \overline{r^2_{exp}}|}{\overline{r^2_{exp}}} \tag{4}$$

HyperStudy (Altair®, 2024.1) was employed as a DoE tool to systematically vary the DEM input parameters (CED, μ_s, μ_r) [38]. It also provides a suite of regression and optimization algorithms to build surrogate models that predict likely optimal parameter sets that best reproduce the experimental flow metrics. These anticipated input sets have to be validated by running their corresponding DEM simulation.

Table 4
Simulations with random combinations of μ_s, μ_r, and CED.

Test	μ_s	μ_r	CED (J/m^3)
A	0.9	0.1	30,000
B	0.3	0.3	50,000
C	0.1	0.1	100,000
D	0.1	0.9	150,000

3. Results

3.1. Calculating surface and cohesion properties of wood powder

3.1.1. Calibration of the spruce and poplar samples

Rotating drum experiments were conducted at the laboratory for both wood samples. Poplar powder exhibited better flowability than that of spruce because it had lower $\sigma(Area)_{exp}$ (0.78% < 1.2%) and higher $\overline{r^2}_{exp}$ (0.989 > 0.95).

Based on these results, the calibration of the powder target input parameters was executed. First, spruce sample was evaluated, in which a series of simulations was conducted by varying the three parameters: sliding friction coefficient (0.1, 0.367, 0.633, 0.9), rolling friction coefficient (0.1, 0.367, 0.633, 0.9), and cohesion energy density (0, 30, 70, 100, 130, 150 kJ/m^3). Each combination of these parameter values was tested, resulting in a total of 96 simulations (*full factorial: 4x4x6*).

As mentioned before, the goal was to identify which (CED, μ_s, μ_r) set gives the minimum value of the objective function $f(\text{CED}, \mu_s, \mu_r)$ while respecting the condition of the maximum accepted difference between the simulated and experimental results for each of $\overline{Area}, \sigma(Area), and\ \overline{r^2}$. Using HyperStudy, the optimal combinations with different optimization algorithms are presented in Table 5. The used algorithms were (*i*) the Adaptive Response Surface Method (ARSM) for sample-efficient local refinement, (*ii*) the Global Response Surface Method (GRSM) to combine surrogate-based optimization with global exploration, and (*iii*) a Genetic Algorithm (GA) for gradient-free global search [39]. This trio of optimizers is well-suited to DEM calibration because the error landscape has many local minima and abrupt changes; surrogate-based ARSM and GRSM limit the number of costly DEM runs, while the GA provides broad, gradient-free exploration to avoid getting trapped in suboptimal regions. However, these sets of values are only predicted by model fitting, so each parameter set must be verified with running a full DEM simulation.

After running simulations using the results of Table 5, the best input combination that had the minimum objective function was $\mu_s = 0.1$, $\mu_r = 0.367$, and CED = 130 kJ/m^3. This simulation took 3.9444 h of computing time. The corresponding flow metrics are $\overline{Area_{sim}}$ = 55.1% ($\overline{Area_{exp}}$ = 54.5%), $\sigma(Area)_{sim}$ = 1.1% ($\sigma(Area)_{exp}$ = 1.2%), and $\overline{r^2}_{sim}$ = 0.957 ($\overline{r^2}_{exp}$ = 0.95).

Regarding poplar calibration, 48 simulations were conducted, representing a full factorial of the following sets of values: μ_s (0.1, 0.367, 0.633, 0.9), μ_r (0.1, 0.367, 0.633, 0.9), and CED (70, 100, 130 kJ/m^3). Less number of CED values were simulated here because after calibrating the spruce sample, we gained insights about the influence of some inputs on the flow metrics. The optimal suggested combination of parameters suggested by HyperStudy are shown in Table 6. After running

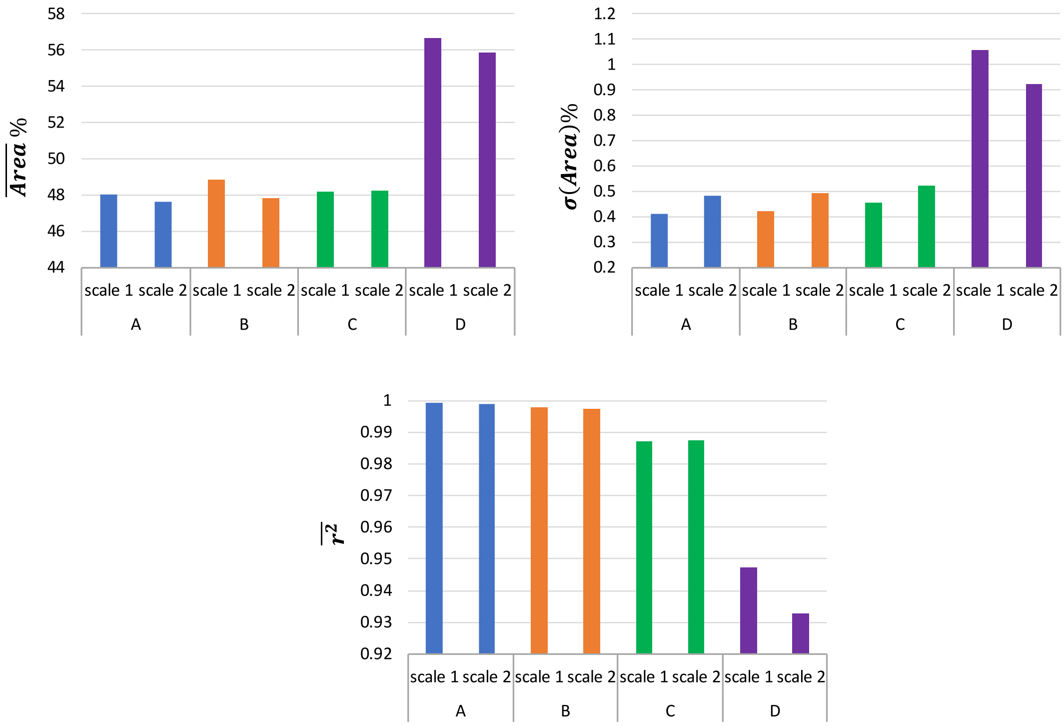

Fig. 7. Comparison of the powder flow descriptors between non-scaled (1) and scaled (2) simulations for the 4 tests (A to D).

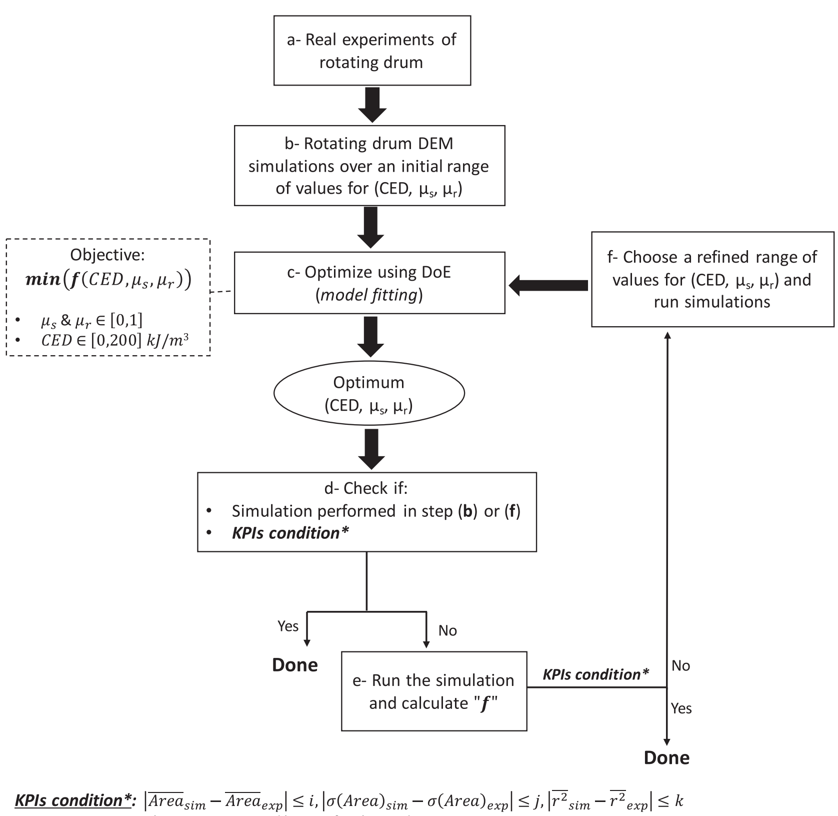

Fig. 8. Flow chart of the calibration procedure of (CED, μ_s, μ_r) using flow descriptors from the rotating drum test (real vs. DEM simulations).

simulations using these sets of values, the best combination giving the minimum value of the objective function was $\mu_s = 0.1$, $\mu_r = 0.77$, and CED $= 100$ kJ/m^3. This simulation took 4.362 h of computing time. The corresponding flow metrics are $\overline{Area}_{sim}$= 60.9% ($\overline{Area}_{exp}$= 60.2%), $\sigma(Area)_{sim}$= 0.79% ($\sigma(Area)_{exp}$= 0.78%), and $\overline{r^2}_{sim}$= 0.981 ($\overline{r^2}_{exp}$= 0.989).

Fig. 9 represents images from real rotating drum experiments of spruce and poplar samples on one hand and snapshots of their

Table 5
Optimal (μ_s, μ_r, CED) combinations for spruce.

Optimisation method	μ_s	μ_r	CED (kJ/m^3)	f
ARSM	0.1	0.367	130	0.102
GRSM	0.1514491	0.4114751	150	0.252
GA	0.1511339	0.4138336	150	0.252

Table 6
Optimal (μ_s, μ_r, CED) combinations for poplar.

Optimisation method	μ_s	μ_r	CED (kJ/m^3)	f
ARSM	0.1	0.772	100	0.033
GRSM	0.1	0.9	100	0.038
GA	0.78	0.63	37.5	0.222

corresponding DEM simulations, using the calibrated values of μ_s, μ_r, and CED, on the other hand.By qualitative comparison, the experimental and simulated powder flow behavior appeared similar for both wood species.

3.1.2. Comparison of the results of the wood powder samples

The cohesion energy density for spruce was 130 kJ/m^3, greater than that of poplar which was 100 kJ/m^3. Thus, the spruce sample is more cohesive, and this explains the fact that it had lower flowability than poplar. The circularity value of the particles of both samples was calculated, such that spruce had an average $\overline{\psi} = 0.496$ with a span $= 0.335$, while poplar had $\overline{\psi} = 0.579$ with a span $= 0.272$. As previously explained, this means that spruce particles possess more surface roughness, and these micro-pores increase the adhesive contact points. After taking images of the powder using scanning electron microscopy (SEM), spruce powder appeared to be more fibrous while poplar was smoother with more uniformity in shape (Fig. 10). It is important to note that the cohesion between particles is also affected by their chemical composition, and these two wood species have distinct ligno-cellulosic compositions (cellulose, hemicellulose, lignin), affecting their intrinsic surface energy and intermolecular attractive forces [40].However, this aspect is beyond the scope of this study.

With respect to the rolling friction coefficient, μ_r for poplar (0.772) was higher than that of spruce (0.367). Poplar sample contained slightly longer particles where the ratio $\frac{\overline{F_{max}}}{F_{min}}$is 2.95 for poplar and 2.71 for spruce, which hinders free rolling. However, this difference in μ_r cannot be

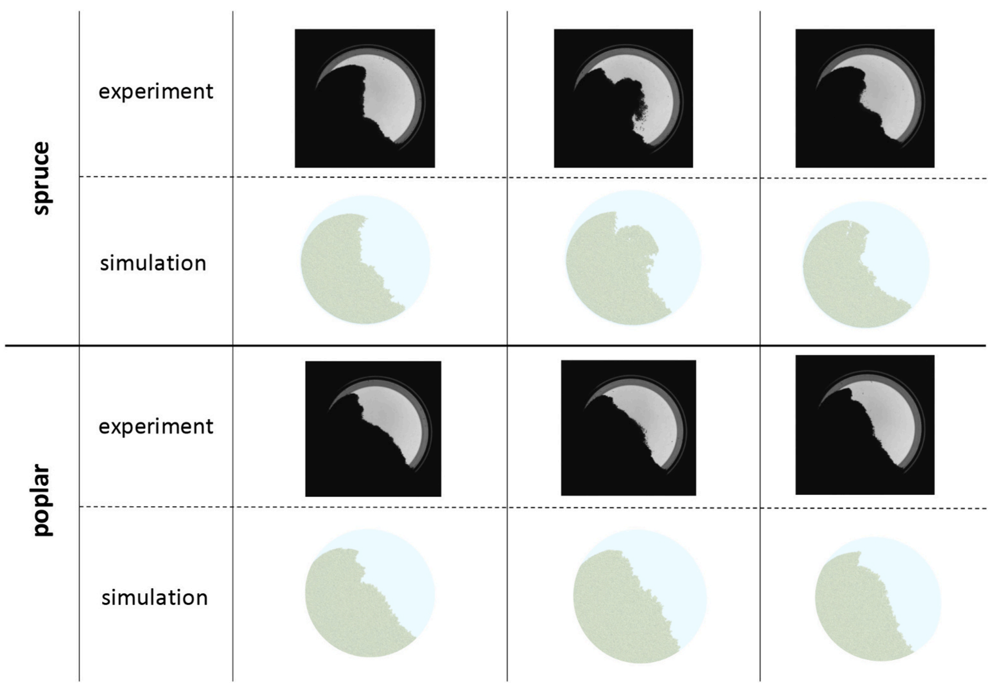

Fig. 9. Typical snapshots of the rotating wood powders from the experimental results and calibrated DEM simulations at different instants.

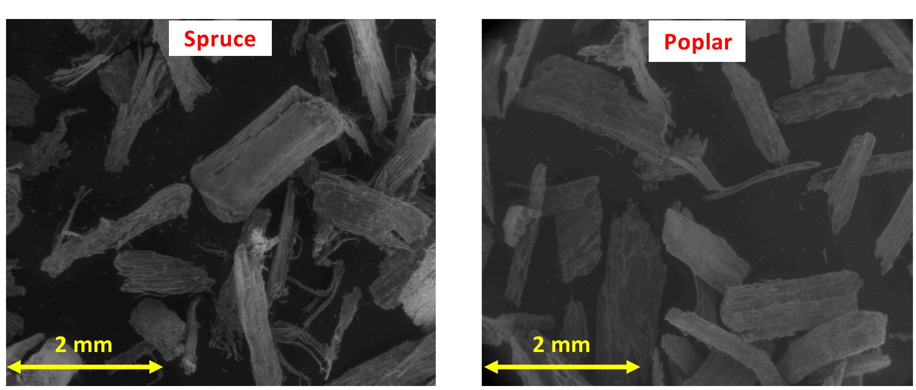

Fig. 10. SEM images of the wood powders (Magnification x50).

solely explained by the aspect ratio; μ_r is an effective parameter that encompasses multiple mechanisms, including particle shape irregularity, particle elongation, surface roughness, contact multiplicity, and elastic dissipation.

3.2. Influence of surface and cohesion properties on the powder bed behavior

3.2.1. Sensitivity analysis

Pareto plots were produced following a DoE–based sensitivity analysis (Fig. 11). For each output, the plots rank the influence of the input parameters individually (μ_s, μ_r, and CED), reporting the contribution (%) derived from standardized regression coefficients [41]. Bars with greater height indicate a stronger influence on the corresponding output, and parameters are displayed in descending order. This sensitivity analysis was chosen to be done based on spruce data, since spruce calibration involved a larger simulation campaign (96 simulations for spruce vs. 48 simulations for poplar), providing a denser sampling of the parameter space and therefore a more reliable basis to infer parameter sensitivity trends.

As illustrated by the previous plot, CED is the most influential parameter for the three outputs ($\overline{Area}$: 55.77%, $\sigma(Area)$: 51.84%, $\overline{r^2}$: 73.31%). The cohesion energy controls the inter-particle attraction, so it directly affects how easily powder particles detach and flow. The rank of the influence of μ_s and μ_r differed between the outputs, μ_s had a higher impact than μ_r for $\overline{Area}$, but it is the opposite case for $\sigma(Area)$ and $\overline{r^2}$. These results cannot be assumed to be quantitatively generalizable to other powders without further investigation.

The cohesion energy density dominates flow behavior, especially for fibrous, irregular particles. Needle-like particles have larger contact surface areas, which amplify van der Waals and capillary forces, contributing to higher effective cohesion [42]. This leads to irregular and non-linear surface formation of the powder bed (lower $\overline{r^2}$), bigger bed build up as the cohesion effect challenges the gravity effect (higher $\overline{Area}$), and more fluctuation in the area while rotating with the formation of blocks and clumps (higher $\sigma(Area)$).

Fig. 12 focuses on the CED contribution by plotting the variation of the three rotating drum outputs ($\overline{Area}$, $\sigma(Area)$, $\overline{r^2}$) with respect to CED for all the combinations of (μ_s, μ_r). It illustrates the general trend for the CED impact as explained earlier, and also shows that higher CED widens the scattering of the outputs.

As observed previously in Fig. 11, the sliding friction coefficient showed a moderate influence on $\overline{Area}$ (28.88%) and $\sigma(Area)$ (23.34%), whereas low impact on $\overline{r^2}$ (9.70%). For elongated particles, sliding is not always a primary motion due to interlocking. Still, it plays a role during the powder initial displacement and spreading in the drum, interaction with the drum wall, and rearrangement during cascading. Hence, it affects the projected area size and variability. But once a bed structure forms, sliding friction has less control over surface shaping — that is more governed by how particles stick (CED) or roll (μ_r). So, while μ_s controls how particles start to move, it is less critical for forming a smooth, coherent surface slope.

The rolling friction coefficient had the least influence on $\overline{Area}$ (15.35%), while moderate influence on $\sigma(Area)$ (24.82%) and $\overline{r^2}$ (16.99%) (Fig. 11). μ_r is critically important for elongated particles, which don't roll easily like spheres, such as the irregular-shaped wood powder. Thus, it affects the stability of the powder surface layers and their reorganization during the flow ($\sigma(Area)$) and plays a role in the development of angular pile slopes or irregular surface profiles ($\overline{r^2}$) especially when CED is lower, since particles can either roll into place or destabilize the surface.

3.2.2. Effect of CED, μ_s, μ_r on unconfined powder flowability

The effect of the powder properties (μ_s, μ_r, CED) on its unconfined flowability was explored. As previously stated, powder unconfined flowability refers to the ability of a bulk powder to flow freely under gravity with minimum presence of external confinement or applied stress. In our previous study, we reached the best flow descriptors to evaluate this aspect [5], and one of them is the $\sigma(Area)$ which will be used in this analysis. The lower the fluctuation of the area $\sigma(Area)$, the better the powder flowability. The results plotted in Fig. 12 are not sufficient because the effects of the two friction coefficients are hidden.

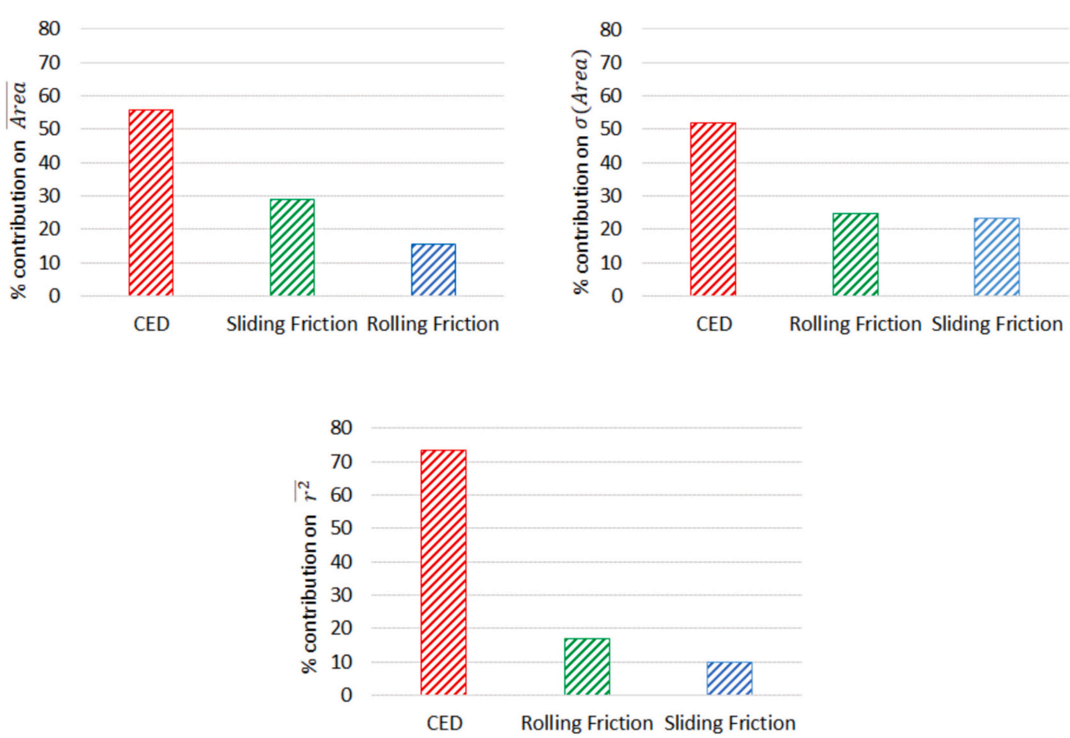

Fig. 11. Pareto plots of input-parameter influence on flow descriptors of spruce powder in rotating drum.

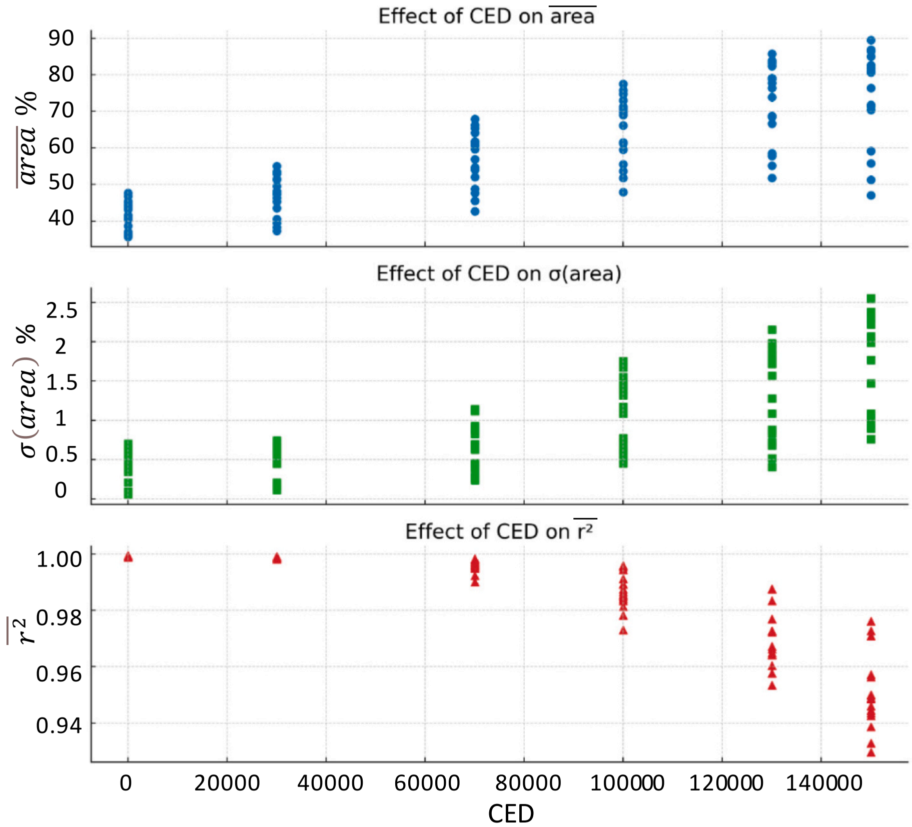

Fig. 12. Effect of CED on the spruce powder dynamics in a rotating drum; for each CED value, the results of all the (μ_s, μ_r) combinations are plotted.

Consequently, using the results of the simulations performed for calibrating the spruce powder in DEM, heatmaps were plotted to illustrate the effect of μ_s, μ_r, and *CED* on $\sigma(Area)$ (Fig. 13).

As a general trend across all these heatmaps, $\sigma(Area)$ increases with higher CED, so poor powder flowability is attained. Higher rolling friction also increases $\sigma(Area)$, especially at high CED values, thus it reduces flowability. Concerning the effect of sliding friction, for $\mu_s = 0.1$ (low), flowability is generally better (more green zones), and at low CED and low rolling friction, $\sigma(Area)$ is lowest, which represents the ideal conditions. When the sliding friction increases, there is an overall shift in the heatmaps colors towards yellow and red, which indicates poor flowability. Also, the system becomes more sensitive to changes in CED and μ_r, $\sigma(Area)$ starts increasing even at lower CED and rolling friction levels.

Finally, the results point to a general deterioration of powder flowability with increased CED and friction; however, the evolution is not monotonic. Instead, the response of the powder bed varies based on how the parameters interact, demonstrating that no single parameter governs solely the flowability. Therefore, the combined effect of CED and both friction coefficients is synergistic rather than additive. CED is the main factor affecting powder flowability in our case study, could differ for other powder types, that's why spruce, possessing higher CED, had lower flowability than poplar, which had higher μ_r. It's worth mentioning that both samples belong to the same sieve cut.

4. Conclusion

Powder flowability is a fundamental aspect for solids handling—affecting dosing accuracy, throughput stability, segregation control, and safety. Wood powders add complexity due to irregular, fibrous particle shapes, hygroscopicity, and chemical heterogeneity, making prediction strongly material-specific. Several factors influence powder flowability, including particle size, shape, and density; this study focused on parameters that are more difficult to measure directly—those linked to surface and cohesive properties rather than morphological properties—especially for lignocellulosic materials such as wood. Two powders were studied, spruce as softwood and poplar as hardwood.

The cohesion energy density (CED), rolling friction coefficient (μ_r), and sliding friction coefficient (μ_s) between particles for the two wood powders were estimated by DEM calibration against real experiments. The interest of this contribution lies in the novel calibration framework, not in a universal parameter set. The main objective of this work is to introduce and validate a practical calibration method to extract key microscopic surface interaction parameters—CED, μ_s, μ_r—from new macroscopic powder-bed dynamics descriptors obtained using a single device (rotating drum), rather than relying on multiple separate tests. The compared descriptors calculated from the rotating powder bed are the projected area ($\overline{Area}$) with its fluctuation ($\sigma(Area)$) and the irregularity of the surface profile ($\overline{r^2}$). Modeling wood powders is challenging as they exhibit fibrous, elongated shapes with significant non-uniformity, so the particles were modeled using clumps of multi-spheres with different sizes of clumps per sample. Regarding the contact model used for forces implementation and calculation by DEM, the *Hertz Mindlin* contact model was used with *Type C Rolling Friction* and *Linear Cohesion V2*. After conducting a set of simulations, the corresponding calibrated parameters for spruce were μ_s=0.1, μ_r=0.367, *CED*=130 kJ/m3, while those of poplar were μ_s=0.1, μ_r=0.772, *CED*=100 kJ/m3. The impact of μ_s, μ_r, and *CED* on the powder dynamic behavior was also analyzed. Increasing the cohesion energy density enhances the attractive forces between particles, leading to stronger agglomeration and reduced powder flowability. Similarly, higher sliding and rolling friction coefficients increase interparticle resistance and energy dissipation, thereby limiting particle mobility and hindering smooth flow.

These determined surface and cohesion particle properties represent effective DEM parameters that can be used for evaluating unconfined

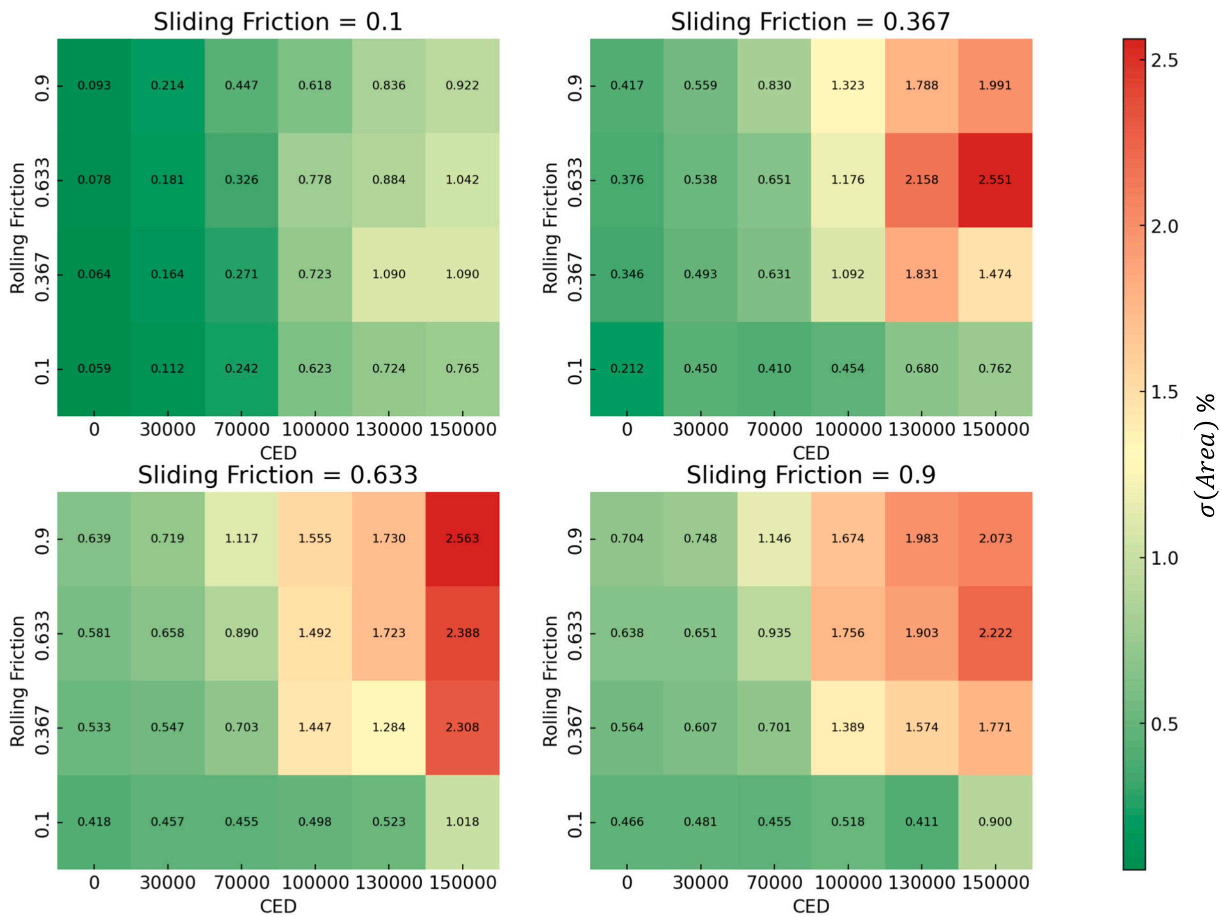

Fig. 13. Heatmaps presenting the effect of CED and μ_r on σ(area), each corresponding to a value of μ_S (spruce powder).

powder flow. Future work could tackle several aspects, such as studying the influence of moisture content on CED, transferring the calibrated parameters to non-scaled particle size, and evaluating the applicability of these parameters on other devices like the shear cell.

CRediT authorship contribution statement

Reem Khazem: Writing – review & editing, Writing – original draft, Software, Methodology, Investigation. **Julien Colin:** Writing – review & editing. **Hao Shi:** Writing – review & editing, Validation, Methodology, Investigation. **Joel Casalinho:** Writing – review & editing. **Dingena Schott:** Writing – review & editing, Validation. **François Puel:** Writing – review & editing, Supervision.

Declaration of competing interest

The authors declare that they have no known competing financial interests or personal relationships that could have appeared to influence the work reported in this paper.

Acknowledgements

The authors would like to acknowledge the French Ministry of Higher Education and Research for funding the doctoral work, and the Erasmus+ Program for providing additional support for the research stay of Reem KHAZEM in TU Delft in the Netherlands.

Data availability

Data will be made available on request.

References

[1] A. Joppich, H. Salman, Wood powder feeding, difficulties and solutions, Biomass Bioenergy 16 (1999) 191–198, https://doi.org/10.1016/S0961-9534(98)00082-8.
[2] F. Thevenon, M. Marchand, M. Grateau, H. Demey, A. Chatroux, P. Pons De Vincent, A. De Ryck, T. Melkior, Energy requirements to produce fine powders of raw and torrefied wood at pilot scale, and characterization of their flowability, Biomass Bioenergy 152 (2021) 106196, https://doi.org/10.1016/j.biombioe.2021.106196.
[3] J. Yang, T. Bell, M. Pasha, Evaluation of a uniaxial powder tester and comparison with an annular shear tester, Powder Technol. 403 (2022) 117405, https://doi.org/10.1016/j.powtec.2022.117405.
[4] A. Neveu, F. Francqui, G. Lumay, Measuring powder flow properties in a rotating drum, Measurement 200 (2022) 111548, https://doi.org/10.1016/j.measurement.2022.111548.
[5] R. Khazem, J. Colin, J. Casalinho, J. Pachón-Morales, F. Puel, Flowability of granular materials in a rotating drum: investigation of relevant flow descriptors, Powder Technol. (2025) 121231, https://doi.org/10.1016/j.powtec.2025.121231.
[6] B.J. Ennis, G. Tardos, R. Pfeffer, A microlevel-based characterization of granulation phenomena, Powder Technol. 65 (1991) 257–272, https://doi.org/10.1016/0032-5910(91)80189-p.
[7] H. Shi, R. Mohanty, S. Chakravarty, R. Cabiscol, M. Morgeneyer, H. Zetzener, J. Ooi, A. Kwade, S. Luding, V. Magnanimo, Effect of particle size and cohesion on powder yielding and flow, Kona Powder Part. J. 2018 (2018), https://doi.org/10.14356/kona.2018014.
[8] W. Nan, M. Pasha, T. Bonakdar, A. Lopez, U. Zafar, S. Nadimi, M. Ghadiri, Jamming during particle spreading in additive manufacturing, Powder Technol. 338 (2018) 253–262, https://doi.org/10.1016/j.powtec.2018.07.030.
[9] W. Nan, M. Pasha, U. Zafar, S. Nadimi, W.P. Goh, M. Ghadiri, Characterisation of gas-atomised metal powders used in binder jet 3D printing, Powder Technol. 436 (2024) 119471, https://doi.org/10.1016/j.powtec.2024.119471.
[10] DEM Modelling of Segregation in Granular Materials: A Review. https://www.jstage.jst.go.jp/article/kona/41/0/41_2024017/_article/-char/ja/, 2025 (accessed September 19, 2025).
[11] A.M. Joshua, G. Cheng, E.V. Lau, Soft matter analysis via atomic force microscopy (AFM): a review, Appl. Surf. Sci. Adv. 17 (2023) 100448, https://doi.org/10.1016/j.apsadv.2023.100448.

[12] J. Ai, J.-F. Chen, J.M. Rotter, J.Y. Ooi, Assessment of rolling resistance models in discrete element simulations, Powder Technol. 206 (2011) 269–282, https://doi.org/10.1016/j.powtec.2010.09.030.
[13] S. Mohammadi-Jam, K.E. Waters, Inverse gas chromatography applications: a review, Adv. Colloid Interf. Sci. 212 (2014) 21–44, https://doi.org/10.1016/j.cis.2014.07.002.
[14] J. Pachón-Morales, H. Do, J. Colin, F. Puel, P. Perré, D. Schott, DEM modelling for flow of cohesive lignocellulosic biomass powders: model calibration using bulk tests, Adv. Powder Technol. 30 (2019) 732–750, https://doi.org/10.1016/j.apt.2019.01.003.
[15] B.D. Jenkins, A.L. Nicuşan, A. Neveu, G. Lumay, F. Francqui, J.P.K. Seville, D. Weston, D. Werner, C.R.K. Windows-Yule, The sensitivity of powder characterization tool measurements to particle properties, Powder Technol. 448 (2024) 120231, https://doi.org/10.1016/j.powtec.2024.120231.
[16] C. Coetzee, O.C. Scheffler, Comparing particle shape representations and contact models for DEM simulation of bulk cohesive behaviour, Comput. Geotech. 159 (2023) 105449, https://doi.org/10.1016/j.compgeo.2023.105449.
[17] Z. Tasnim, Q. Chen, Y. Xia, A. Hamed, J. Klinger, R. Navar, B. Davis, Discrete element modeling of irregular-shaped soft pine particle flow in an FT4 powder rheometer, Powder Technol. 450 (2025) 120437, https://doi.org/10.1016/j.powtec.2024.120437.
[18] J. Horabik, M. Bańda, V. Vozarova, L. Kubik, M. Stasiak, DEM modeling of wood sawdust compaction and breakage strength of pellets determined in diametral compression test, Int. Agrophys. 37 (2023) 51–58, https://doi.org/10.31545/intagr/156086.
[19] D. Dickmann, National Research Council Canada, Poplar Council of Canada, Poplar Council of the United States, Poplar Culture in North America, NRC Research Press, Ottawa, 2001.
[20] Y.H. Jung, H.J. Cho, J.-S. Lee, E.W. Noh, O.K. Park, K.H. Kim, Evaluation of a transgenic poplar as a potential biomass crop for biofuel production, Bioresour. Technol. 129 (2013) 639–641, https://doi.org/10.1016/j.biortech.2012.12.074.
[21] QICPIC, Sympatec Anal. Part. Size Shape. https://www.sympatec.com/en/particle-measurement/sensors/dynamic-image-analysis/qicpic, 2025 (accessed June 3, 2025).
[22] Particle Shape, Sympatec Anal. Part. Size Shape. https://www.sympatec.com/en/particle-measurement/glossary/fundamentals-of-particle-characterisation/particle-shape, 2025 (accessed September 22, 2025).
[23] Welcome to Altair EDEM. https://2024.help.altair.com/2024.1/edem/index.htm, 2025 (accessed September 9, 2025).
[24] H. Hertz, On the contact of elastic solids, J. Reine Angew. Math. 92 (1882) 156–171.
[25] R.D. Mindlin, H. Deresiewicz, Elastic spheres in contact under varying oblique forces, J. Appl. Mech. 20 (2021) 327–344, https://doi.org/10.1115/1.4010702.
[26] A. Hadi, H. Shi, Y. Pang, D. Schott, Identification of dominant DEM parameters for multi-component segregation during heap formation, hopper discharge and chute flow, Powder Technol. 444 (2024) 119985, https://doi.org/10.1016/j.powtec.2024.119985.
[27] W. Nan, W. Xuan, Z. He, H. Hou, Z. Sun, W. Li, Analysis of the screw feeding process in powder-based additive friction stir deposition, Powder Technol. 455 (2025) 120791, https://doi.org/10.1016/j.powtec.2025.120791.
[28] Linear Cohesion V2 Model. https://2024.help.altair.com/2024.1/edem/topics/creator_tree_physics/the_linear_cohesion_v2_model_r.htm, 2025 (accessed September 22, 2025).
[29] H. Ma, L. Zhou, Z. Liu, M. Chen, X. Xia, Y. Zhao, A review of recent development for the CFD-DEM investigations of non-spherical particles, Powder Technol. 412 (2022) 117972, https://doi.org/10.1016/j.powtec.2022.117972.
[30] B. El-Kassem, N. Salloum, T. Brinz, Y. Heider, B. Markert, A multivariate regression parametric study on DEM input parameters of free-flowing and cohesive powders with experimental data-based validation, Comput. Part. Mech. 8 (2021) 87–111, https://doi.org/10.1007/s40571-020-00315-8.
[31] H. Kruggel-Emden, S. Rickelt, S. Wirtz, V. Scherer, A study on the validity of the multi-sphere Discrete Element Method, Powder Technol. 188 (2008) 153–165, https://doi.org/10.1016/j.powtec.2008.04.037.
[32] Fluid Mechanics - Hydrodynamics, Flow, Pressure, Britannica, 2025. https://www.britannica.com/science/Archimedes-principle (accessed June 6, 2025).
[33] M. Rackl, F. Top, C.P. Molhoek, D.L. Schott, Feeding system for wood chips: a DEM study to improve equipment performance, Biomass Bioenergy 98 (2017) 43–52, https://doi.org/10.1016/j.biombioe.2017.01.003.
[34] W. Callister, D. Rethwisch, Materials Science and Engineering (an Introduction), 9th ed., 2013. https://anupturnedworld.wordpress.com/wp-content/uploads/2016/06/callister-materials-science-and-engineering.pdf.
[35] S.J. Burns, P.T. Piiroinen, K.J. Hanley, Critical time step for DEM simulations of dynamic systems using a Hertzian contact model, Int. J. Numer. Methods Eng. 119 (2019) 432–451, https://doi.org/10.1002/nme.6056.
[36] M.J. Mohajeri, R.L.J. Helmons, C. van Rhee, D.L. Schott, A hybrid particle-geometric scaling approach for elasto-plastic adhesive DEM contact models, Powder Technol. 369 (2020) 72–87, https://doi.org/10.1016/j.powtec.2020.05.012.
[37] J. Mellmann, The transverse motion of solids in rotating cylinders—forms of motion and transition behavior, Powder Technol. 118 (2001) 251–270, https://doi.org/10.1016/S0032-5910(00)00402-2.
[38] Altair Software and Hardware 2024.1 Release Notes. https://2024.help.altair.com/2024.1/hwdesktop/altair_help/topics/release_notes/rn_2024_1_software_and_hardware_r.htm, 2025 (accessed September 30, 2025).
[39] A. Forrester, A. Sobester, A. Keane, Engineering Design Via Surrogate Modelling: A Practical Guide, 2008, https://doi.org/10.1002/9780470770801.
[40] F.P. Liu, T.G. Rials, J. Simonsen, Relationship of wood surface energy to surface composition, Langmuir 14 (1998) 536–541, https://doi.org/10.1021/la970573y.
[41] What is a Pareto Chart? Analysis & Diagram, ASQ, 2025. https://asq.org/quality-resources/pareto?srsltid=AfmBOorZNKGjl7dIbWsXYIkmuNfiqTHC-hD9l51G1maJD3WIpyDO7ZuI (accessed September 30, 2025).
[42] M. Mariano, General aspects of powder rheology applied to pharmaceutical formulations, Drug Discov. Today 29 (2024) 103976, https://doi.org/10.1016/j.drudis.2024.103976.